Temperature Gradient Image Analysis to Optimize an Ultrafast Regeneration of Boron–Oxygen-Related Defects

Sebastian Roder , Tim Niewelt , Andreas Brand, Jale Schneider, and Jan Nekarda

Abstract—In this study, we introduce a temperature screening image analysis to investigate the temperature dependence of boron–oxygen-related defect regeneration achieved by using one sample. For that purpose, we induce a temperature gradient in a single sample over a broad temperature range in our laser-based rapid thermal processing furnace, while other influencing factors are kept constant. Spatially resolved measurements of the temperature during the regeneration process (thermographic images) and photoluminescence (PL) images at different boron–oxygen-related defect states are recorded. By a pixelwise assignment of the PL images to the temperature image, the effectiveness of the regeneration process in terms of regeneration completeness is evaluated for each pixel. In this experiment, we investigate the temperature dependence of a boron–oxygen-related defect regeneration in a temperature range of 100–500 °C for different treatment times of 2–30 s at an illumination intensity of 100 kW/m². Thereby, we determine the temperature regimes that allow for efficient regeneration for the respective regeneration parameter set with a single sample. The results can be used for industrial optimization of a boron–oxygen-related defect regeneration process. Furthermore, this technique can also be applied to other temperature-dependent process optimizations and even fundamental research.

Index Terms—Boron–oxygen-related (BO) defect, process optimization, regeneration, temperature screening method, ultrafast regeneration (UFR).

I. INTRODUCTION

FUNDAMENTAL understanding or empirical knowledge of the temperature dependence of a process step in a solar cell production is often essential for efficient process development or optimization. An example for a process with a strong impact of temperature is the stabilization of boron–oxygen-related (BO)

defects. This process can be performed in an industrial solar cell production with electrical injection and heating or a laser-based regeneration tool [1], [2]. Commonly, a routine is used, where a set of samples is treated with different temperatures in order to screen the parameter space [1], [3]. Afterward, the process efficacy is assessed, and the sequence is iterated until sufficient data are gathered. Screening a broad temperature range with at least one sample per temperature can, thus, be a material- and time-consuming approach.

Regarding BO defect regeneration with the ultrafast regeneration (UFR) technology [2], a screening of the temperature field is crucial to provide an optimized process at treatments times less than 10 s. The process is intended to transfer BO defects into the so-called regenerated state [4], [5]. The potential completeness of this process—addressed here as regenerability—not only depends on the regeneration process itself, but is also affected by various parameters of the cell concept and preceding treatments. For example, the firing temperature and profile of the formation of the rear contact have a significant impact, and therefore, the regeneration process needs to be optimized independently for each given solar cell process. For a detailed discussion of the influencing factors, we refer to the review paper by Hallam *et al.* [6] and the references therein.

In this work, we suggest an approach to cover a broad temperature range on a single sample. We introduce the temperature screening imaging analysis to investigate the temperature dependence of BO defect regeneration with a laser-based rapid thermal processing (RTP) furnace, including a temperature imaging system. The emphasis in this article is to reduce the time and material consumption for process optimizations regarding the temperature and to get a complete picture of the influence of a wide temperature range. However, this approach is transferable to other temperature-dependent process optimizations and even fundamental research. The requirement is the technical possibility to induce a temperature gradient within the sample and have a spatially resolved quantitative measurement of the target quantity—such as the efficacy of the process.

II. EXPERIMENTAL DETAILS

A. Sample Preparation

The experiment was performed on industrial boron-doped Czochralski-silicon precursors (156.6-cm side length and 160-μm thickness) featuring a phosphorus emitter and silicon

oxynitride (SiO_xN_y) back-side and silicon nitride (SiN_x) front-side passivation layers. The precursors are sourced from an industrial manufacturer with a bulk resistivity of 1.7 $\Omega\cdot$cm and an emitter sheet resistivity of $\sim$100 Ω/sq. We applied a full-area aluminum (Al) back-side metallization by screen printing, which ensures a similar thermal behavior as finished solar cells. Thereafter, a fast firing step at a peak temperature of 850 °C is applied in an industrial conveyor belt furnace. We omitted the contact opening process because no actual contact was necessary and such localized features might add noise to the imaging-based evaluation.

B. Experimental Setup for the Regeneration Process

The used offline RTP furnace applies a full-area 980-nm laser illumination for heating and excess carrier generation. The maximum illumination intensity across the 156 $\times$ 156 mm² sample area is 270 kW/m². Most of the photon energy of 1.27 eV is used for electron–hole pair generation in silicon, which allows for a high excess carrier injection at elevated temperatures. In this experiment, we apply constant illumination intensity across the sample and adjust an air flow in a way that creates the intended broad temperature variation. To control temperature, the air flow is applied parallel to the sample surface plane. The main consideration for inducing a temperature gradient in the sample is to change the local cooling properties of the air flow. This is achieved by using an air jet with a widen-up cross section of the air flow, which reduces the velocity along the sample and, thus, reduces the cooling effect. Additionally, other thermal effects such as natural convection also have an influence on the induced temperature gradient. Due to the small thickness and the high thermal conductivity of the samples, no significant inhomogeneity in the vertical direction is expected. To further increase the temperature range that can be achieved on a single sample, two independent air flows separated by an air partition wall are used [see Fig. 1(a)]. An infrared (IR) camera (INFRATEC, VarioCam HD research 600) is used to capture temperature images with a recording frequency of 60 Hz, a resolution of 640 $\times$ 480 pixels, and a specified measurement accuracy of $\pm$1%. The IR camera signal is calibrated to the investigated temperature range by a thermocouple attached to the metalized sample back side. Thereby, the metalized back side ensures that no IR radiation is transmitted through the sample. Fig. 1(b) and (c) shows an exemplary temperature image during the plateau stage of a regeneration process ($t_{LASER,ON}$ = 10 s and P_{LASER} = 100 kW/m²), a cross section to illustrate the induced temperature gradient and a temperature profile at specific points.

The *in situ* temperature monitoring allows us to investigate the specific temperature profiles at any spot. Some examples of temperature–time profiles for a 30-s illumination process are shown in Fig. 1(c) for the spots indicated in Fig. 2(b) (thermographic image). The cooldown after the process is realized via a strong air flow perpendicular to the sample that is turned ON when the laser and the parallel air flow are switched OFF. This ensures a rapid cooldown after the process. For simplification of the evaluation of the temperature dependence of the regeneration
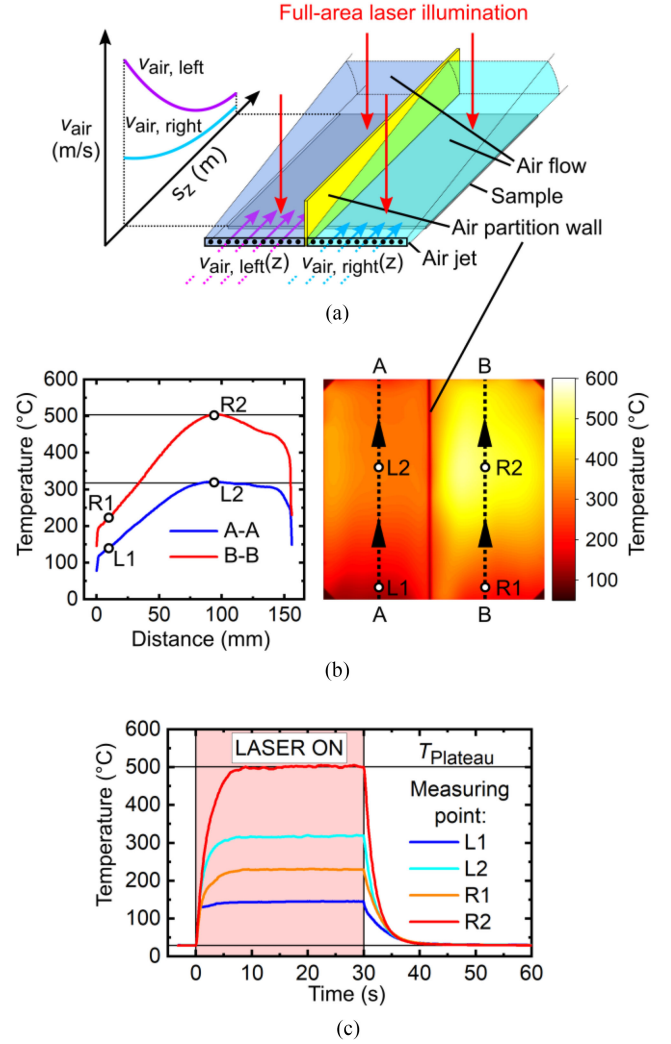

Fig. 1. (a) Schematic drawing of the experimental setup for inducing a temperature gradient. Two independent controllable air jets, separated by an air partition wall, are used. Air speed is reduced along the sample by a widen-up cross section of the air flow. The qualitative air speed along the direction of the air flow is illustrated for the left (purple) and right (cyan) air flow. (b) Temperature profile for the line scans A-A and B-B indicated in the temperature image. Temperature image taken during the temperature plateau stage illustrates the temperature distribution achieved by air jets. Application of an air flow partition wall allows for a temperature range of 100–500 °C on one sample with homogeneous illumination. (c) Temperature profiles for exemplary spots on a sample during a UFR process with a laser-ON-time of 30 s.

process, the plateau temperature $T_{Plateau}$ is determined for each pixel, as illustrated in Fig. 1(c) for the spots L1, L2, R1, and R2. Here, $T_{Plateau}$ represents the average temperature of a pixel during the temperature saturation phase by which the temperature fluctuates. The standard deviation of $T_{Plateau}$ during the saturation phase is determined to be $\pm$5K. It should be noted that higher temperatures were observed to saturate later, but we expect minor impact of the ramp-up time for subsequently long processes.

C. Approach and Measurement Routine

The main concept of the approach is to induce a temperature gradient into the sample while keeping other influencing factors
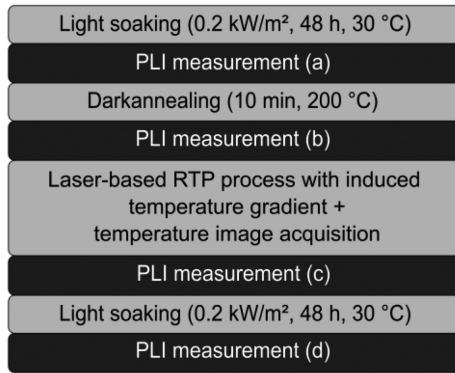
Fig. 2. Routine to characterize the temperature-dependent efficacy of a BO defect regeneration. The intention of each process step (gray) is to transfer the BO defect in a defined state. After each process step, the samples are measured with a lifetime-calibrated PLI performed in a so-called MODULUM tool [measurements (a)–(d)].

Fig. 3. iVoc images after the respective process to transfer the BO defect in the different defect states. (a) Degraded: faint ring structure indicates crystal-growth-related striations of the dopant concentration or the presence of oxide precipitates. (b) Annealed: increased iVoc values compared to the degraded state. (c) After UFR: similar iVoc values compared with the annealed state. (d) After UFR + light soaking: light soaking reveals that some areas of the wafer were stabilized significantly less effective when compared to the iVoc image after the process. Thin vertical line in the wafer center due to the shading caused by the air flow partition wall.

like illumination intensity constant. Afterward, the measured process temperatures are correlated with the efficacy of the process in terms of the regeneration completeness (RC) [2], which is described in detail in Section II-D. Therefore, two spatially resolved characterization techniques are used: 1) *in situ* temperature imaging with an IR camera in order to measure the different temperatures on one sample during the BO defect regeneration process and 2) spatially resolved lifetime-calibrated photoluminescence imaging (PLI) performed in a so-called MODULUM tool [7]. Details on the calibration can be found in [8]. To characterize the BO defect, we use a characterization routine, whereby the samples are measured after each process, which brings the sample into a defined defect state (degraded, annealed, and regenerated; see, e.g., [9]). The intention of the regeneration process is to reach the regenerated state with its stability to module operation and low recombination activity. The process sequence in Fig. 2 lists the performed steps and indicates the performed measurements.

After firing, the samples are subjected to a light-soaking step at 30 °C under illumination with 0.2 kW/m² (fluorescent tube) for 48 h to fully activate BO defects. Thus, the present defects should be all in the degraded state for the first PLI measurement [see Fig. 2(a)] (performed at 1-sun equivalent illumination and calibrated to a lifetime image via modulated photoluminescence). Then, samples are subjected to a dark annealing step at 200 °C for 10 min on a hotplate to transfer the BO defects to the annealed state. The samples are transferred to the imaging setup in the dark to avoid reactivation of the defects [see Fig. 2(b)]. After the second PLI measurement, the sample is treated with the BO defect regeneration process in the aforementioned laser-based RTP furnace. Regenerating from the annealed state describes a worst-case scenario, since the regeneration of the BO defect appears to be a transition from the degraded to the regenerated state, and therefore, the defect must be activated by the process at first [10]. During the regeneration process, a temperature gradient from 100 to 500 °C is induced across the sample, while an IR camera acquires the temperature. After this process, BO defects are in an undefined state, as
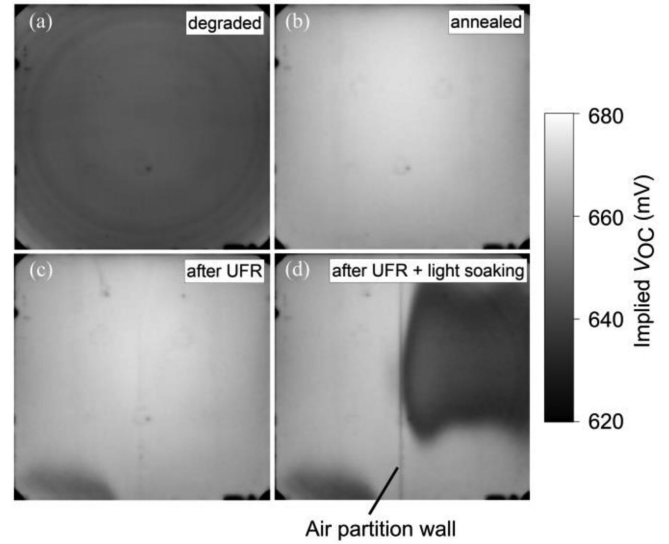
depending on the local process parameters, they will distribute on degraded, annealed, and regenerated state. To investigate this and thereby examine the impact of temperature, another PLI measurement [see Fig. 2(d)] is followed by a subsequent second light-soaking step to reactivate all defects that were in annealed state after the regeneration treatment. Note that potentially present iron contaminations are believed to be in interstitial iron (Fe$_i$) configuration for all measurements. We have also tested our samples with Fe-imaging, which gave no indication of significant iron concentration (see the left in Fig. 7).

By comparing the four PLI measurements, information on local process efficiency can be determined. We choose to use an approach, which is derived from [2], to analyze RC by calculating implied open-circuit voltages (iVoc) images from the lifetime-calibrated PLI measurements. Note that the investigation of the process in terms of the RC based on iVoc does not fully account for the injection dependence introduced by BO defects. Derivation of a quantity such as the normalized defect density (Nt*) would be superior in this regard. However, this would require information at a fixed minority carrier density, which cannot be measured precisely with spatial resolution in the annealed state of the samples. Therefore, we choose to analyze RC based on iVoc, which reflects the dominant impact of BO defects on cell performance. Exemplary in Fig. 3 for one sample, the four iVoc images in its different states are shown.

In the degraded state [see Fig. 3(a)], a faint ring structure indicates crystal-growth-related striations of the dopant concentration or the presence of oxide precipitates. After the light-soaking step, the iVoc image [see Fig. 3(d)] reveals that some areas of the
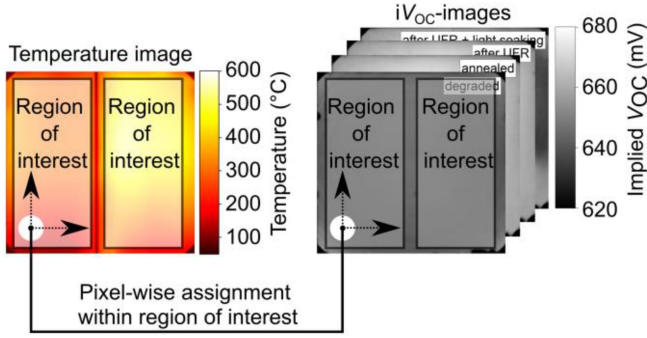
Fig. 4. Pixelwise assignment of temperature image to i*V*oc images. Each temperature pixel is assigned to four PLI pixels from the PLI measurements in the different states. Furthermore, an ROI is defined to exclude experimentally misleading features such as scratches or the wafer edge.

Fig. 5. i*V*oc over plateau temperature (T_{Plateau}) in the different states of the routine. Each temperature image pixel represents four corresponding i*V*oc image pixels in the different states, limited to values to the degraded state from 642 to 643 mV and in the annealed state from 662 to 663 mV.

wafer were stabilized significantly less effective when compared with the i*V*oc image after the process [see Fig. 3(c)]. Another prominent feature, revealed by light soaking, is the thin vertical line in the wafer center due to the shading caused by the air flow partition wall.

D. Assessment of Temperature-Dependent Process Efficacy

The temperature dependence is analyzed via a pixelwise assignment of the temperature image (here: T_{Plateau} image) to the i*V*oc images. Fig. 4 illustrates the assignment process and the investigated region of interest (ROI) in our experiment. The output of the IR camera was rescaled from its native resolution of 640×480 pixels via linear interpolation to the 1024×1024 pixel resolution of the MODULUM PLI system. Note that due to the given high number of pixels, the ROI can be chosen conservatively to avoid the impact of experimentally misleading features such as scratches or the wafer edge.

The alignment of the images was supported by a wafer edge detection and perspective correction algorithm. The rescaling and alignment to the wafer edges can introduce additional uncertainty beyond the measurement precision. The wafer edges in the temperature image can be detected within a 10-pixel precision, which leads to a 2-D error of 14.2 pixels. In our experiment, the highest temperature gradient observed was 0.6 K/pixel (after rescaling). Hence, we believe the uncertainty to be 8.5 K for assigning a temperature image pixel to a photoluminescence (PL) image pixel as a worst case. The error due to a possible misalignment of the PL images is assumed to be negligible, since the wafer edges of the PL images can be precisely detected due to the high contrast between the sample and the underlying sample holder. After the alignment of the images to each other, a pixelwise assignment is performed. Hereby, each temperature image pixel represents four corresponding i*V*oc image pixels in the different states. Fig. 5 shows an example of 15 000 pixels restricted to the range of 642–643 mV in the degraded image and 662–663 mV in the annealed image.

Fig. 5 compares the measured i*V*oc of 15 000 exemplary pixels in all BO defect states (red—degraded state, blue—annealed state, black—after UFR, and green—after UFR + light soaking)
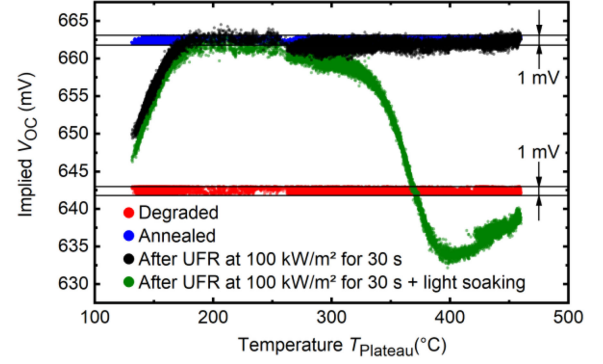
plotted versus the reached plateau temperature (T_{Plateau}). The data from this single wafer covered a temperature range of 150–450 °C. When plotting all data points within this type of graph, artefacts can be obtained as the degraded state featured a slight lateral gradient and data scatter. This results in artifacts when plotting the raw spatially resolved voltage data over T_{Plateau} with its spatial distribution. To tackle this, the process efficacy is analyzed as mentioned above in terms of *RC* that is defined as follows [2]:

$$RC = \frac{\text{i}V\text{oc}_{\text{After UFR+light soaking}} - \text{i}V\text{oc}_{\text{Deg}}}{\text{i}V\text{oc}_{\text{Ann}} - \text{i}V\text{oc}_{\text{Deg}}}. \quad (1)$$

Hereby, an *RC* of 1 represents a complete regeneration. Conversely, an *RC* of ≤ 0 represents absent regeneration, where i*V*oc does not improve or even degrades due to the process. Because of the relative nature of *RC*, this calculation corrects the aforementioned artifacts so that all data points within the ROI can provide meaningful evaluation. Thus, evaluation to *RC* also normalizes the data and thereby accounts for the initial lateral inhomogeneity of the wafer mentioned above. If the absolute signal in initial state affects the investigated process, care should be taken to avoid artefacts, e.g., by restricting evaluation to initially homogeneous regions if possible. Fig. 6 depicts the average value of *RC* binned to 1 K and the standard deviation of the about 700 000 data points in the ROI indicated in Fig. 4.

The annealed (blue-marked) and the degraded (red-marked) states are 1 and 0 by definition, respectively. For the black plot, the calculated *RC* after (1) is referred to as apparent regeneration completeness (RC_{App}), as the sample was not yet exposed to a light-soaking step after the BO defect regeneration process. After the light-soaking step, the stabilized BO defects are revealed for the temperature range. This type of graph is the basis for the discussion and the followed optimization of an UFR process.

E. Application for Process Optimization

To demonstrate a process optimization using temperature gradient image analysis (TGIA), we vary the treatment time of the BO defect regeneration process. Here, other process relevant parameters, such as illumination intensity, are kept constant.
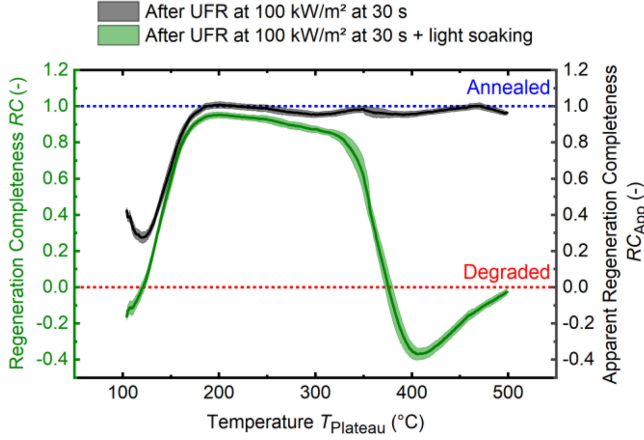
Fig. 6. *RC* over the plateau temperature (T_{Plateau}) for all data points within the ROI. The condition after UFR process (black) is referred to as RC_{App}, as the sample has not yet been exposed to light. The mean value is plotted as a line and the standard deviation in the respective color as an area. Annealed (blue) and degraded (red) states are illustrated as dotted lines.
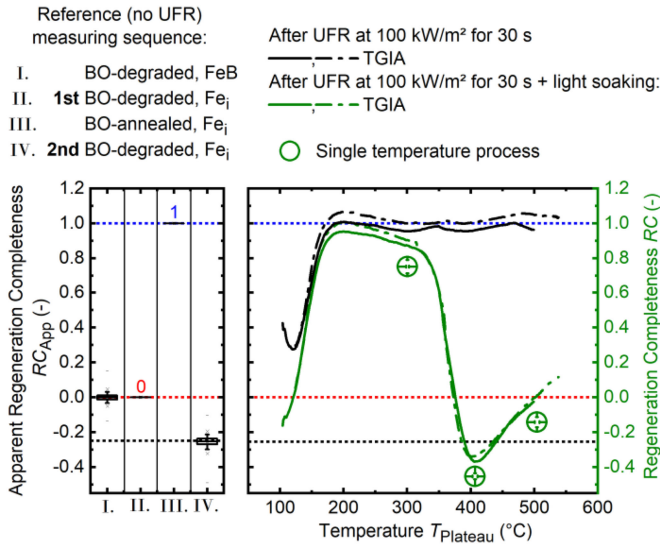

Fig. 7. (Left) Impact of the preprocessing steps on the samples that are not treated with an UFR process is shown. Measuring sequence is from I to IV. For the non-UFR-treated samples (black), an RC_{App} is used. Fe imaging gave no indication of significant iron concentration by comparison of states I and II. After annealing (III) and an additional light-soaking step, an *RC* of –0.25 can be observed in state IV. (Right) *RC* over the plateau temperature (T_{Plateau}) for two samples (solid- and dashed-dotted lines) in the state after UFR + light soaking (green) is shown. For non-light-soaked samples (black), an RC_{App} is used. Furthermore, quartered samples are treated with a single process temperature (green-marked circles) to assess the transferability of the results of this method to single temperature processes.

We performed regeneration processes with this method at an illumination intensity of 100 kW/m² for illumination times of 30, 10, 5, and 2 s (see Fig. 8). Additionally, TGIA processes were performed, in which the air flow, ensuring a rapid cooldown, is not switched ON. We are investigating this because, in our experimental setup, a variation of the cooling rate with T_{Plateau} and lateral position is expected. The processes were performed
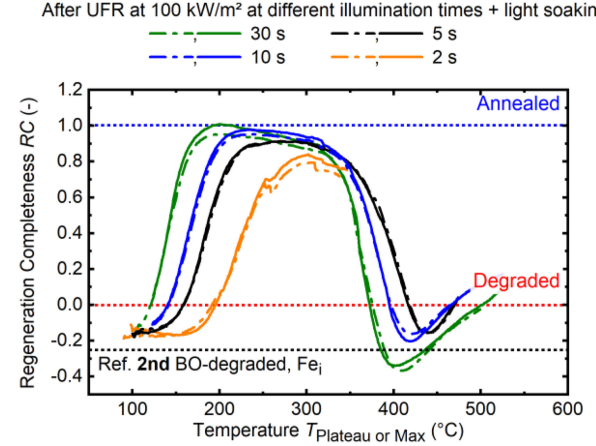

Fig. 8. *RC* over the plateau temperature (T_{Plateau}) for different illumination times at an illumination intensity of 100 kW/m². A shift of the curves to higher temperatures is observed when decreasing the illumination time from 30 to 2 s. Additionally, the annealed state (blue), the degraded state (red), and the impact of the preprocessing steps on non-UFR-treated samples followed by a second light-soaking step (black) are illustrated as dotted lines.

at an illumination time of 30 and 5 s at an illumination intensity of 100 kW/m².

Furthermore, quartered samples (7.8 × 7.8 cm²) were treated with a single process temperature to evaluate the transferability of the results of this method to single temperature processes. Treatments at temperatures of 300, 405, and 500 °C with an illumination intensity of 100 kW/m² and an illumination time of 30 s are applied.

III. RESULTS AND DISCUSSION

A. Process Example and Transferability to Single Temperature Processes

Fig. 7(right) shows results of the same BO defect regeneration process (100 kW/m² and 30-s illumination time) for two samples to demonstrate the reproducibility of the approach. The single data points at 300, 405, and 500 °C represent results on quartered samples treated at these temperatures. Furthermore, the impact of the different preprocessing steps on the samples is illustrated (see the left in Fig. 7).

A regeneration process at given parameters (here, temperature, illumination intensity, and cooling down rate) results in a mixture of the three possible states of BO defects (degraded, annealed, and regenerated state) directly after the UFR process. After an additional light-soaking step, the defects, formerly in annealed state, will be activated, while the regenerated state is not affected. Therefore, the measurements in final state reveal in which temperature range the BO defect regeneration was successful. On the right of Fig. 7, values of $RC < 0$ were found in the temperature range of 100–120 °C and from 375 to 500 °C. We found that this cannot be attributed to the impact of potential iron contamination as indicated by pairing/splitting testing on sister samples shown in the left part of Fig. 7. However, a dark annealing at 200 °C for 10 min followed by a light-soaking step at 30 °C and 0.2 kW/m² (with no UFR processing in between)

resulted in a decrease of RC by –0.25 (corresponding to 6.3 mV) compared with the initial state. This behavior could be explained by a change of the amount of BO defects during the dark annealing. Walter *et al.* show that sample processing affects the concentration of available BO defects, and subsequent thermal treatments such as dark annealing at moderate temperatures can change the equilibrium [11]. The timescales indicated by Walter *et al.* are longer than those in our experiments (e.g., about 50 h at 200 °C compared with the 10 min we applied), but similar effects of a shifted equilibrium could explain the RC values below 0 that we observed. However, since our samples were most likely treated with different preprocesses and have different thermal histories, this may alter the kinetics of the equilibrium reaction. Another explanation could be that the precursors were partially regenerated before the process and destabilized during the dark annealing step. However, we assume that this is less likely, as the firing step ($T_{\text{Firing, Peak}} = 850$ °C) should have already destabilized such defects.

In the temperature range of 100–122 °C, a decrease of the black curve is observed, which is most likely caused by the thermally increased degradation rate (see [9] and references therein). No significant BO defect regeneration or annealing reaction is observed in this temperature range. The regeneration reaction becomes more prominent in the temperature range from 100 to ~160 °C: the regeneration rate is thermally activated and the necessary proceeding defect activation is rapid (see [10]). In the temperature range of 160–320 °C, a high RC can be reached. A fraction of defects ends up in annealed state, which results in a decrease after a light-soaking step. Thereby, we observed $\Delta RC = -0.05$ for T_{Plateau} of ~200 °C and a slightly stronger effect toward higher temperatures, which could be due to an increasing destabilization reaction (see [6] and references therein). For temperatures above $T > 322$ °C, the destabilization and annealing reactions dominate the state ratio after the process, which results in a high RC_{App} but low actual RC. We observe the lowest iVoc around $T_{\text{Plateau}} = 405$ °C with an $RC = -0.37$ followed by an increase of RC toward higher temperatures. This increase could be related to another purely thermal pathway for deactivation of BO defects besides the pathway with annealing and illumination, as suggested by Nampalli *et al.* [12]. They proposed a four-state model based on the three-state model of Herguth and Hahn [13], where a thermal treatment can dissociate defect precursors of BO defects. As shown by Nampalli *et al.*, a decrease in normalized defect concentration is observed from the lowest temperature studied at 450–632 °C. This appears to be a similarity to our results, as the RC increases at 405 °C and continues to increase up to the highest temperature studied of 500 °C. Therefore, this could be a possible explanation for the increase at a temperature of $T > 405$ °C besides another possible hydrogen-related mechanism during the regeneration process. Given the RC_{App} close to 1 in the temperature range $T > 322$ °C, the light and elevated temperature-induced defect (LeTID) can be excluded to have a significant impact on the results. The difference between the apparent RC_{App} and RC is revealed by the light soaking close to room temperature and, thus, more likely caused by BO defects than LeTID.

Furthermore, the cooldown phase can have an impact on the overall regeneration result. In our experimental setup, a variation of the cooling rate with T_{Plateau} and lateral position is expected that would not necessarily apply to an industrial process. A too long cooldown phase could lead to a possible destabilization of the regenerated defects due to the presence of elevated temperatures in the absence of illumination [5]. In addition, as suggested by Nampalli *et al.*, the cooldown phase might have an impact on the deactivation of BO defects through the purely thermal pathway for $T > \sim 450$ °C [12]. To investigate this impact on our process, we have analyzed another regeneration process using the TGIA method representing a worse case. In this case, we turned OFF the air flow usually ensuring a rapid cooldown after the process. The cooling rate then reduces significantly, e.g., from 250 to 115 °C/s for T_{Plateau} at 500 °C (evaluated in the temperature range of 400–500 °C). No significant difference of the TGIA curves was observed between the different cooldown phases over the full temperature range. Thus, we assume that slight variations of the rate do not affect the overall regeneration result in the processes we investigated.

Additionally, quartered samples, as mentioned above, were treated with a single process temperature to assess the transferability of the results of this method to single temperature processes. The regeneration processes at temperatures of 300, 405, and 500 °C are shown in the right part of Fig. 7 as green points with its standard deviation. Thereby, the single temperature processes have a shift of $\Delta RC \approx -0.1$ compared with the results of the TGIA method. This deviation could be due to an imprecise transfer of process relevant parameters of the regeneration process (temperature profile including the cooldown phase and illumination intensity). The origin of the shift between TGIA and single process temperatures is still under investigation and could also be related to the high-temperature gradients induced in the sample compared with the single temperature processes. However, the qualitative behavior of the resulting curves of this method fits quite well with single temperature processes. For optimization purposes, it is important to reproduce the concrete conditions of the regeneration process proposed by this method.

B. Example of Process Optimization With TGIA

Fig. 8 shows the performed regeneration processes with TGIA at an illumination intensity of 100 kW/m² for illumination times of 30, 10, 5, and 2 s. Note that with shorter process times than 10 s, it is not possible to reach the saturation temperatures for all temperatures anymore. Consequently, a smaller temperature range can be covered. The temperature profile of those pixels can be described as a heat-up ramp to the maximum temperature (T_{Max}) that can be reached within the illumination time.

A shift of the curves to higher temperatures was observed when decreasing the illumination time from 30 to 2 s. In the temperature range of 100–200 °C, longer process times support higher RC. This could be due to the low regeneration and degradation rates at these temperatures. At higher temperatures of around 400 °C, a shift of the low points to lower RC values and lower temperatures can be noted. As mentioned above, this
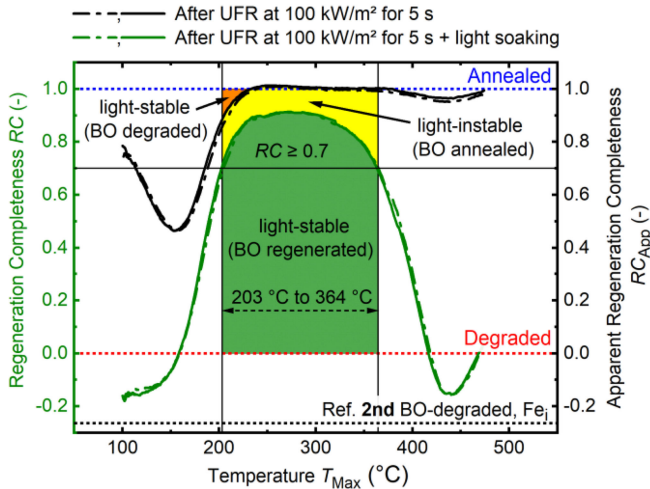
Fig. 9. Process window for an UFR process at 5 s and 100 kW/m². Green-, yellow-, and orange-marked areas describe the BO regenerated, annealed, and degraded states, respectively. For the process requirement $RC > 0.7$, a process window regarding the temperature from 203 to 364 °C is determined.

could be related to a change of the amount of the BO defects or a hydrogen-related mechanism during the regeneration process.

Finally, to use this method and the resulting curves for a time-optimized regeneration process, the process requirement defines which curve should be used. For instance, the process window for an illumination time of 5 s and a targeted RC above 0.7 is shown in Fig. 9.

The green, yellow, and orange areas illustrate the regenerated, annealed, and degraded shares, respectively. The process window reaching the targeted RC is the temperature range of 203–364 °C. In this case, choosing a target temperature of 283.5 °C would provide a large temperature deviation and yield. However, for an accurate process transfer to an industry process, a precise transfer of the process relevant parameters is required when using this technique as an optimization method.

IV. CONCLUSION

With the introduced imaging analysis, it is possible to investigate the temperature dependence of BO defect regeneration with a laser-based RTP furnace in a broad temperature range by using only one sample. Within this study, a temperature range of 100–500 °C is investigated on a single solar cell precursor. The resulting curves are in good agreement to processes featuring a single temperature across a sample. Thereby, it is essential to reproduce the specific regeneration conditions with its impact factors, such as temperature profile (including cooling down phase) and illuminations intensity. Hence, with this approach, it

is possible to carry out a broad temperature range screening for process development or optimization with a potential reduced material and time consumption. In this experiment, a shift of the maximum achievable RC to lower temperatures could be observed at longer process times. Furthermore, this technique can be used for the analysis of other temperature-dependent processes if the target value can be spatially resolved with an imaging technique, and the technical possibility exists to induce a temperature gradient in the sample.

ACKNOWLEDGMENT

REFERENCES

[1] J. Ye et al., "Study on the electrical injection regeneration of industrialized B-doped Czochralski silicon PERC solar cells," Int. J. Photoenergy, vol. 2019, Jun. 2019, Art. no. 5357370.

[2] A. A. Brand et al., "Ultrafast in-line capable regeneration process for preventing light induced degradation of boron-doped p-type Cz-silicon PERC solar cells," in Proc. 33th Eur. Photovolt. Sol. Energy Conf. Exhib., Amsterdam, The Netherlands, 2017, pp. 382–387.

[3] S. Wilking, C. Beckh, S. Ebert, A. Herguth, and G. Hahn, "Influence of bound hydrogen states on BO-regeneration kinetics and consequences for high-speed regeneration processes," Sol. Energy Mater. Sol. Cells, vol. 131, pp. 2–8, Dec. 2014.

[4] A. Herguth, G. Schubert, M. Kaes, and G. Hahn, "Avoiding boron-oxygen related degradation in highly boron doped Cz silicon," in Proc. 21th Eur. Photovolt. Sol. Energy Conf., Munich, Germany, 2006, pp. 530–537.

[5] A. Herguth, G. Schubert, M. Kaes, and G. Hahn, "A new approach to prevent the negative impact of the metastable defect in boron doped Cz silicon solar cells," in Proc. IEEE 4th World Conf. Photovolt. Energy Conf., Waikoloa, HI, USA, 2006, pp. 940–943.

[6] B. Hallam et al., "Eliminating light-induced degradation in commercial p-type Czochralski silicon solar cells," Appl. Sci., vol. 8, 2018, Art. no. 10.

[7] H. Höffler et al., "Review and recent development in combining photoluminescence- and electro-luminescence-imaging with carrier lifetime measurements via modulated photoluminescence at variable temperatures," in Proc. 37th Eur. Photovolt. Sol. Energy Conf. Exhib., Lisbon, Portugal, 2020, pp. 264–276.

[8] J. A. Giesecke, M. C. Schubert, B. Michl, F. Schindler, and W. Warta, "Minority carrier lifetime imaging of silicon wafers calibrated by quasi-steady-state photoluminescence," Sol. Energy Mater. Sol. Cells, vol. 96, pp. 1011–1018, Mar. 2011.

[9] T. Niewelt, J. Schon, W. Warta, S. W. Glunz, and M. C. Schubert, "Degradation of crystalline silicon due to boron–oxygen defects," IEEE J. Photovolt., vol. 7, no. 1, pp. 383–398, Jan. 2017.

[10] P. Hamer et al., "Investigations on accelerated processes for the boron–oxygen defect in p-type Czochralski silicon," Sol. Energy Mater. Sol. Cells, vol. 145, pp. 440–446, Feb. 2016.

[11] D. C. Walter, R. Falster, V. V. Voronkov, and J. Schmidt, "On the equilibrium concentration of boron-oxygen defects in crystalline silicon," Sol. Energy Mater. Sol. Cells, vol. 173, pp. 33–36, Dec. 2017.

[12] N. Nampalli et al., "Multiple pathways for permanent deactivation of boron-oxygen defects in p-type silicon," Sol. Energy Mater. Sol. Cells, vol. 173, pp. 12–17, Dec. 2017.

[13] A. Herguth and G. Hahn, "Kinetics of the boron-oxygen related defect in theory and experiment," J. Appl. Phys., vol. 108, Dec. 2010, Art. no. 114509.